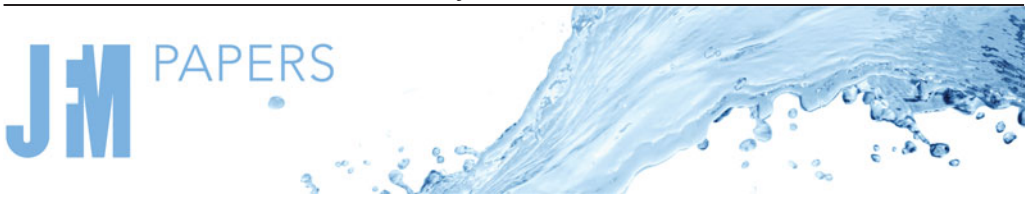
J. Fluid Mech. (2021), *vol*. 920, A42, doi:10.1017/jfm.2021.430



Flow structures and heat transport in Taylor–Couette systems with axial temperature gradient

X.-Y. Leng[1], D. Krasnov[2], B.-W. Li[3] and J.-Q. Zhong[1],†

[1]School of Physics Science and Engineering, Tongji University, 200092 Shanghai, PR China

[2]Fakultät für Maschinenbau, Technische Universität Ilmenau, Postfach 100565, 98684 Ilmenau, Germany

[3]School of Energy and Power Engineering, Dalian University of Technology, 116024 Dalian, PR China

(Received 26 December 2020; revised 27 March 2021; accepted 12 May 2021)

We investigate the heat transfer and coherent structures in Taylor–Couette (TC) flows that undergo thermal convection driven by an axially applied temperature gradient. Direct numerical simulations are performed in a Rayleigh number range $10^6 \leq Ra \leq 3 \times 10^8$ for Prandtl number $Pr = 4.38$ and with the shear Reynolds number up to $Re = 10^4$. When the rotation number R_f increases, the flows undergo a transition from buoyancy-dominated ($R_f < 1$) to shear-dominated convection ($R_f > 1$). In the buoyancy-dominated regime with weak rotations, the flow features are similar to those in Rayleigh–Bénard (RB) convection with large-scale plumes emanating from the thermal boundary layers. In this regime, the Re-dependence of heat transport Nu is sensitive to Ra. We find that for low Ra, Nu decreases with increasing Re and becomes independent of Re at high Ra. In the shear-dominated regime, the flow structures are characterised by Taylor vortices (TVs), which effectively enhance the heat transport. With sufficiently high Reynolds number for $2000 < Re \leq 10\,000$, the flow structures are dominated by turbulent TVs, and the transport scaling laws of heat and angular velocity fluxes become independent of buoyancy. We report that in this turbulent regime the axial heat-transport scaling ($Nu \sim Re^{0.578\pm0.018}$) is consistent with the scaling of radial angular-momentum transport ($Nu_\omega \sim Re^{0.581\pm0.026}$).

Key words: turbulent convection, Taylor–Couette flow, rotating flows

1. Introduction

Rayleigh–Bénard (RB) convection, a fluid layer heated from below and cooled from above and Taylor–Couette (TC) flow, the flow driven by two independently rotating concentric cylinders, are two canonical models in fluid dynamics. Owing to their simple

† Email address for correspondence: jinqiang@tongji.edu.cn

© The Author(s), 2021. Published by Cambridge University Press

https://doi.org/10.1017/jfm.2021.430 Published online by Cambridge University Press

configurations but abundant connotations, RB and TC systems have been significantly investigated in the last few decades, including early experimental (Taylor 1923; Andereck, Liu & Swinney 1986; Koschmieder 1993) and theoretical works (Chandrasekhar 1981; Grossmann & Lohse 2000; Eckhardt, Grossmann & Lohse 2007) and recent direct numerical simulations (Froitzheim *et al.* 2019; Blass *et al.* 2020), as reviewed by Ahlers, Grossmann & Lohse (2009), Lohse & Xia (2010), Chillà & Schumacher (2012), Fardin, Perge & Taberlet (2014) and Grossmann, Lohse & Sun (2016). As the twins of turbulence research (Busse 2012), the analogy between RB convection and TC flow has been discovered explicitly by Dubrulle & Hersant (2002), and then extended to the formal form (Eckhardt *et al.* 2007) which describes the analogy between the global transport of heat and angular velocity from a unified viewpoint.

Both paradigmatic systems, RB convection and TC flow, present many important features for large-scale flows in geophysical and astrophysical systems (Ji *et al.* 2006; King & Aurnou 2015). In these interdisciplinary areas, one of the key issue is to understand the turbulent transport processes, such as the predictions of heat transport in the Earth's atmosphere and ocean, and the angular momentum transport in an accretion disk.

For many turbulent systems, coherent structures are known to play crucial roles in heat, mass and momentum transport (Bergman *et al.* 2011). For the example of turbulent RB convection, heat transport is implemented by convective plumes and large-scale circulation (LSC) in the bulk flow. Accordingly, previous studies have considered several mechanisms, such as the Coriolis force by global rotation (Zhong *et al.* 2009) and the Lorentz force by imposed magnetic field (Lim *et al.* 2019), showing the pathway to achieving heat-transfer enhancement based on plume manipulation (Chong *et al.* 2017).

Different types of coherent structures may also exist in TC flow. In the low-Reynolds-number regime just above the onset of the first instability, the steady Taylor vortex (TV) has a very small axial dispersion rate until the appearance of waviness, when the molecular diffusion between adjacent vortices is replaced by axially-chaotic advection (Kataoka & Takigawa 1981; Akonur & Lueptow 2002, 2003). At high Reynolds number, analogous to RB convection, the turbulent bulk consists of large-scale TVs and small-scale plumes, which take over the radial transport of angular momentum (Ostilla-Mónico *et al.* 2014; Van Der Veen *et al.* 2016; Froitzheim *et al.* 2019). However, the axial transport of heat and mass has rarely been discussed in turbulent TC systems, and the performance of TVs on axial turbulent transport is still unclear. It is reported in the experiments by Lathrop, Fineberg & Swinney (1992*a*, *b*), that the axial dispersion of a passive scalar is dictated by the same scaling as that of angular momentum flux. This study, therefore, suggests the potential of significant heat-transfer enhancement in TC systems. It is desirable to potentially graft the rotation-induced TV-like structures to a thermal convection and utilise their properties of effective transport to achieve high performance in heat transfer.

Heat transport in turbulent RB convection is carried out mostly by thermal plumes that self-organise into LSCs, and Nu exhibits scaling dependence on Ra which is well predicted by the Grossman–Lohse (GL) theory (Grossmann & Lohse 2000). This scaling dependence of $Nu(Ra)$, however, is scarcely affected when the conventionally control parameters (e.g. Ra and Pr) vary, because the primary flow structures remain. In this paper, we present a numerical study of rotation-induced heat-transport enhancement by RB convection in an annular cell, with the inner cylinder rotating about the central axis. We demonstrate that, thanks to the formation of TVs, the global axial heat transfer can be largely controlled by the inner cylinder, and achieve a steep power-law scaling in the TC-dominated regime. We find a transition from the RB-type (buoyancy-dominated)

https://doi.org/10.1017/jfm.2021.430 Published online by Cambridge University Press

convection to the TC-type (shear-dominated) turbulence, occurring with a noteworthy change of heat-transfer properties. When the TVs become the dominant coherent structures, their meridional rotations sweep away the thermal boundary layers (TBLs) and pump the hot/cold fluids into the bulk that enhances the heat exchange between boundary layers and bulk, leading to the prominent heat-transport enhancement.

In a similar annular system, the flow in a vertical TC flow with radial heating is also a popular research topic, owing to broad practical applications in industry, such as the studies of stability analysis (Yoshikawa, Nagata & Mutabazi 2013; Kirillov & Mutabazi 2017), flow regime (Guillerm *et al.* 2015), radial buoyancy (Kang *et al.* 2017), large aspect ratio effect (Kang, Yang & Mutabazi 2015) and recently experimental works at high Reynolds number (Singh *et al.* 2019). However, unlike the radial temperature gradient that appears in the previously mentioned cases, we consider an axially-destabilised temperature gradient and investigate axial heat, and radial momentum transport simultaneously. To our knowledge, this is the first attempt to study the turbulent transport of heat and angular momentum in such a flow configuration.

The remainder of this paper is organised as follows. Section 2 provides a brief description of the physical model and numerical technology. Section 3 presents results and discussions of the global heat transfer, the angular velocity transport and the diagnosis of flow regime transition. The conclusions and remarks are in § 4.

2. Numerical model

2.1. *Physical model*

The considered three-dimensional flow of an incompressible viscous fluid is contained between two concentric cylinders of radii r_1, r_2 and height h. The inner wall is rotating about z axis (e_z), pointing vertically upward, while gravity g points downwards. The kinematic viscosity ν, thermal expansion coefficient β and thermal diffusivity κ are assumed to be constant. At the point of RB convection, the height of the cylinders, imposed temperature difference of endwalls Δ and free fall velocity $u_f = \sqrt{\beta g \Delta h}$ are introduced as the length, temperature and velocity scales, respectively. Therefore, within the Boussinesq approximation and neglecting viscous heating, the dimensionless Navier–Stokes equations are

$$\frac{\partial \boldsymbol{U}}{\partial t} + (\boldsymbol{U}\cdot\boldsymbol{\nabla})\boldsymbol{U} = -\boldsymbol{\nabla} p + \sqrt{\frac{Pr}{Ra}}\nabla^2\boldsymbol{U} + Te_z + F_{CB}, \quad \boldsymbol{\nabla}\cdot\boldsymbol{U} = 0, \tag{2.1}$$

$$\frac{\partial T}{\partial t} + (\boldsymbol{U}\cdot\boldsymbol{\nabla})T = \frac{1}{\sqrt{PrRa}}\nabla^2 T, \tag{2.2}$$

where t, p and T are, correspondingly, time, pressure and temperature. And $\boldsymbol{U}$ (U_r, U_θ, U_z), are the components of velocity in radial, azimuthal and axial directions for cylindrical coordinates (R, Θ, Z) respectively. The lower case letters (r, θ, z) denote the dimensional coordinates. In (2.1), the term $F_{CB} = -(\beta\Delta)U_\theta^2 Te_r/R$ is the centrifugal buoyancy (Yoshikawa *et al.* 2013; Guillerm *et al.* 2015), and it is demonstrated in Appendix B that this term does not change the results of heat transport in our parameter space. Therefore, in the following analysis, centrifugal buoyancy is neglected.

The Rayleigh number is $Ra = \beta g \Delta h^3/(\nu\kappa)$, and the Prandtl number $Pr = \nu/\kappa$ is fixed at 4.38. The bottom and top endwalls are maintained at fixed temperatures $T_1 = 1$ and $T_2 = 0$, and the two cylinders are set to be thermally insulating where the radial

https://doi.org/10.1017/jfm.2021.430 Published online by Cambridge University Press

temperature gradients are zero, i.e. $\partial T/\partial R|_{R_1,R_2} = 0$. No-slip boundaries are applied for velocities at all walls.

When the inner wall is rotating, to facilitate the comparison with a pure TC problem, the gap width $d = r_2 - r_1$ and the azimuthal velocity of inner wall $u_1 = \omega r_1$ are also introduced, and the Reynolds number is given by $Re = \omega r_1 d/\nu$. The rotation number, defined as the ratio of the inner wall velocity to the free fall velocity $R_f = \omega r_1/\sqrt{\beta g \Delta h}$, is adopted here to measure the relative strength of RB convection and TC flow.

We use a wide gap with the radius ratio $\eta = r_1/r_2 = 0.5$ and the aspect ratio is $\Gamma = h/d = 4$. In response to the input parameters, the global heat flux (Nusselt number) from the hot bottom to the cold top plates is defined as $Nu = \sqrt{Ra\,Pr}\langle U_z T\rangle + \partial\langle T\rangle/\partial Z$. The friction Reynolds number is defined as $Re_\tau = 0.5 u_\tau d/\nu$, where the friction velocity is $u_\tau^2 = -\nu r(\partial\langle u_\theta/r\rangle_{\theta z,t}/\partial r)$ at the inner wall. Hereafter, the chevrons stand for the averaging process, e.g. the volume- and time-averaging $\langle\,\rangle$ or $\langle\,\rangle_{V,t}$ and the azimuthal- and time-averaging $\langle\,\rangle_{\theta,t}$. The chosen four sets of Ra are 10^6, 5×10^6, 4×10^7 and 3×10^8, whereas Re varies in the range of $0 \le Re \le 10^4$.

2.2. *Numerical method*

The equation system is solved using the finite-difference scheme developed by Krasnov, Zikanov & Boeck (2011) and Krasnov *et al.* (2013) and modified for the cylindrical coordinate (Leng *et al.* 2018; Akhmedagaev *et al.* 2020). The numerical scheme is a second-order approximation based on the spatial discretisation, which is nearly fully conservative with regard to mass, momentum and kinetic energy. The second-order explicit Adams–Bashforth/backward-differentiation scheme is employed for the time discretisation. The viscous terms are treated explicitly, and implicit treatment is applied for the diffusion term. At every time step, two Poisson equations, the projection method equation for pressure and the equation for temperature are solved using fast-Fourier transforms in the azimuthal direction and the cyclic reduction direct solver (Adams, Swarztrauber & Sweet 1999). Towards the walls, a clustered grid is implemented using the hyperbolic tangent coordinate transformation.

For each set of simulations we adopt the gradual increasing strategy, which means that, the pure RB convection is used as the initial condition of the rotating case, and then the low-Re flow is used as the initial field for the following high-Re case. All the results presented hereafter are calculated after excluding the initial stage before reaching statistically steady state. The time convergence is checked by comparing the time averages over the whole (Nu) and the last halves (Nu_h) of the simulation; the resulting deviation is less than 3 %. For the temporal resolution, the chosen time step Δt satisfies the Courant–Friedrichs–Lewy (CFL) condition, where the CFL number remains less than 0.5. The total run time for each case (including the initial and averaging stages) is three times greater than the averaging time.

As our considered RB convections include the weakly nonlinear ($Ra = 10^6$) and turbulent regimes ($Ra = 3\times10^8$), we use various grids according to the Rayleigh number. For high Re, the flows enter the TC-dominated regime, and the grids are determined by the Reynolds number. The results of the grid sensitivity study are listed in table 1 in Appendix A. It is shown that, when the meshes double in three directions, the heat transfer Nu and the friction Reynolds number Re_τ change by less than 2 %.

The main results are listed in tables 2–5 in Appendix A. For all our runs, the smallest mean scale is determined by the Batchelor scale of the temperature field

https://doi.org/10.1017/jfm.2021.430 Published online by Cambridge University Press

Ra	Re	$N_\theta \times N_z \times N_r$	Nu	σ_h	σ_{ϵ_T}	Re_τ	t_{u_1}, t_{u_f}
1×10^6	0	$64 \times 65 \times 25$	7.88	1.00	0.98	—	—, 195.63
1×10^6	0	$128 \times 129 \times 33$	7.87	1.00	0.99	—	—, 117.22
1×10^6	500	$128 \times 129 \times 33$	11.70	1.00	0.93	58.90	437.40, 26.13
1×10^6	500	$192 \times 193 \times 49$	11.90	1.00	0.97	59.12	513.58, 30.68
1×10^6	500	$256 \times 257 \times 65$	11.94	1.00	0.98	59.54	600.12, 35.84
5×10^6	0	$64 \times 65 \times 25$	13.69	1.00	0.98	—	—, 56588
5×10^6	0	$96 \times 97 \times 33$	13.77	0.99	0.99	—	—, 246.25
5×10^6	0	$160 \times 161 \times 41$	13.76	0.99	1.00	—	—, 160.94
5×10^6	500	$128 \times 129 \times 33$	11.81	1.00	0.93	59.37	325.34, 43.45
5×10^6	500	$192 \times 193 \times 49$	12.07	1.00	0.97	59.57	657.04, 87.75
5×10^6	500	$256 \times 257 \times 65$	12.16	1.00	0.98	59.98	268.38, 35.84
4×10^7	0	$128 \times 129 \times 33$	25.13	0.99	0.99	—	—, 148.13
4×10^7	0	$192 \times 193 \times 49$	25.29	1.00	0.99	—	—, 488.00
4×10^7	0	$256 \times 257 \times 65$	25.38	0.99	0.99	—	—, 135.06
4×10^7	500	$128 \times 129 \times 33$	23.35	0.99	0.97	62.56	696.23, 263.00
4×10^7	500	$192 \times 193 \times 49$	23.60	0.98	0.99	62.78	432.17, 163.25
4×10^7	500	$256 \times 257 \times 65$	23.77	0.99	1.00	63.19	322.97, 122.00
3×10^8	0	$256 \times 257 \times 65$	45.51	0.99	0.98	—	—, 140.56
3×10^8	0	$384 \times 385 \times 97$	44.28	1.00	1.00	—	—, 684.80
3×10^8	0	$512 \times 513 \times 129$	44.89	0.99	1.00	—	—, 162.00
3×10^8	500	$256 \times 257 \times 65$	45.40	1.00	0.98	69.55	184.33, 190.69
3×10^8	500	$384 \times 385 \times 97$	45.10	0.99	0.99	70.26	158.59, 164.06
3×10^8	500	$512 \times 513 \times 129$	44.90	0.99	0.99	70.34	104.46, 108.06
3×10^8	2000	$256 \times 257 \times 65$	46.45	0.99	0.95	167.08	1201.78, 310.81
3×10^8	2000	$384 \times 385 \times 97$	46.14	0.99	0.98	166.59	548.33, 141.81
3×10^8	2000	$512 \times 513 \times 129$	46.48	0.98	0.98	167.42	674.72, 174.50
3×10^8	4000	$384 \times 385 \times 97$	56.77	0.99	0.97	278.98	633.88, 81.97
3×10^8	4000	$512 \times 513 \times 129$	57.29	0.99	0.97	277.68	437.70, 56.60
3×10^8	4000	$768 \times 769 \times 193$	56.74	0.99	0.98	278.27	399.19, 51.62

Table 1. Summary of results for the grid sensitivity study.

(Batchelor 1959). The mean Kolmogrov and Batchelor scales, respectively, are given by $\langle\lambda_k\rangle = (\nu^3/\langle\epsilon_\nu\rangle)^{1/4}$ and $\langle\lambda_b\rangle = (\kappa^2\nu/\langle\epsilon_\nu\rangle)^{1/4}$, where $\langle\epsilon_\nu\rangle$ is the mean of the turbulent-kinetic-energy dissipation rate (Pope 2000; Stevens, Verzicco & Lohse 2010; Scheel, Emran & Schumacher 2013). Here, with or without weak imposed shear, our cases satisfy the global resolution criterion proposed by Grötzbach (1983), that $(L_{max}/\langle\lambda_b\rangle) < \pi$, where $L_{max} = Max\sqrt[3]{L_r(r,\theta,z)L_\theta(r,\theta,z)L_z(r,\theta,z)}$ is the maximum of the geometric mean of the grid spacing (Emran & Schumacher 2008) and L denotes the grid spacing in each direction. However, at high Reynolds number, the flow enters the TC-dominated regime, $\langle\lambda_b\rangle$ decreases rapidly with increasing kinetic-energy dissipation. Therefore, we increase this criterion to a larger value that does not exceed 3.7 as a concession. This guarantees the ratio of resolution to $\langle\lambda_k\rangle$ is always less than 1.8. Furthermore, at least ten grid points are arranged in the TBLs for all cases, satisfying the grid requirement of TBL for pure RB flow (Shishkina *et al.* 2010). In addition, the exact relation between the thermal dissipation and the global heat transfer is $\langle\epsilon_T\rangle(hu_f^{-1}\Delta^{-2}) = Nu(Ra\,Pr)^{-1/2}$ (Shraiman & Siggia 1990), where $\langle\epsilon_T\rangle$ is the mean thermal dissipation rate. This yields the definition of

https://doi.org/10.1017/jfm.2021.430 Published online by Cambridge University Press

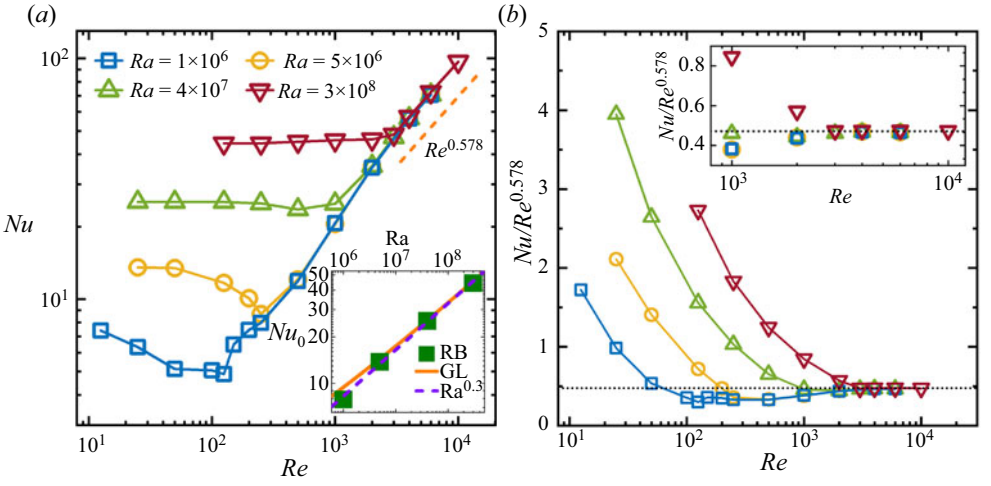


Figure 1. (*a*) Global heat transfer Nu as a function of Re. The orange dashed line denotes a power-law scaling of $Re^{0.578}$. Inset: the non-rotating Nusselt number Nu_0 as a function of Ra. The purple dashed line is the fitting line of $Ra^{0.3}$. (*b*) Compensated Nu as a function of Re. The dotted line is the auxiliary line for $Nu/Re^{0.578} = 0.476$. Inset: an expanded view of the data in the range of $1000 \leq Re \leq 10\,000$.

the relative error measurement $\sigma_{\epsilon_T} = \langle \epsilon_T \rangle (hu_f^{-1}\Delta^{-2})(Ra\,Pr)^{1/2}/Nu$ (Stevens *et al.* 2010; Scheel *et al.* 2013).

3. Results

3.1. *Global heat transport*

Our numerical results of the Nusselt number without rotation, Nu_0 is well described by a power-law scaling $Nu_0 \sim Ra^{0.30}$, which is in agreement with previous experimental results in an annular cell (Zhu *et al.* 2019), and agrees with the GL theory (Stevens *et al.* 2013) over the range of $4 \times 10^7 \leq Ra \leq 3 \times 10^8$ (see inset in figure 1*a*).

Data of Nu obtained for various Ra are presented as functions of Re in figure 1(*a*). With increasing Re, we see that for low Ra the Nusselt number first decreases in the flow regime of weak rotations (low Re). The minimum of heat transport, Nu_m, occurs at a transitional Reynolds number Re^* that depends on Ra. The maximum reduction rate of Nu, $\Delta_{Nu} = 1 - Nu_m/Nu_0$, can be as large as 38 % for the lowest $Ra = 10^6$ used in this study. A decrease in Δ_{Nu} is found when Ra increases and it becomes nearly zero for $Ra = 3 \times 10^8$. In fact for this Ra, Nu becomes nearly independent of Re in this buoyancy-dominated regime ($Re < Re^*$). When $Re \geq Re^*$, flows turn into the shear-dominated regime, where $Nu(Re)$ increases prominently with increasing Re. When $Re > 2000$, we note that the heat-transport scaling approaches a steep power-law $Nu \sim Re^{\gamma}$ with $\gamma = 0.578 \pm 0.018$, and both the scaling exponent and prefactor are independent of Ra, as shown in figure 1(*b*). Such a power-law scaling of heat transport persists up to the maximum Reynolds number ($Re = 10^4$) in the present study. As discussed in § 3.3 and shown by figures 5 and 6, the flow enters the turbulent Taylor vortex flow (TTVF) directly when $Re > 2000$, thus we infer that this power law typifies the properties of heat transport in the TTVF state. Meanwhile, $Re = 2000$ should be the demarcation point dividing the shear-dominated regime into the sub-ranges of weakly nonlinear TV flow ($Re^*(Ra) \leq Re \leq 2000$) and turbulent TV flow ($2000 < Re \leq 10\,000$). The present scaling exponent is much less than

https://doi.org/10.1017/jfm.2021.430 Published online by Cambridge University Press

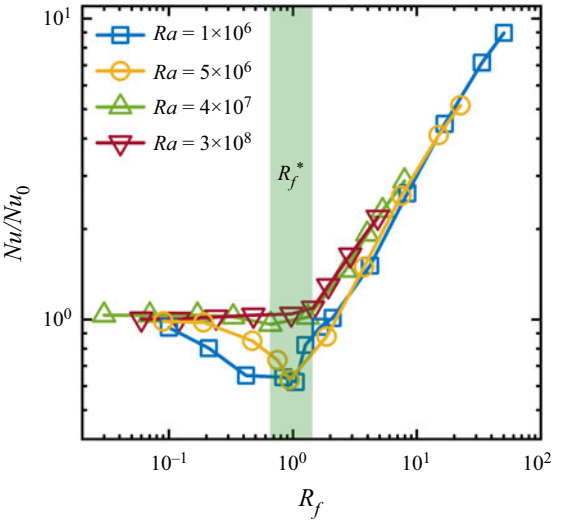


Figure 2. Plot of Nu/Nu_0 as a function of R_f for various Ra. The shaded area indicates the approximate transitional region $0.7 \leq R_f^* \leq 1.4$.

that of the wall-normal heat transfer ($Nu \sim 0.0013Re$) in plane Couette–RB flow (Blass *et al.* 2020). To interpret this difference, further comparisons of the transport properties between TC and plane Couette flows are necessary in the future work.

In figure 2, we present Nu/Nu_0 as a function of R_f. Such a rescaling leads to the converging of the transitional values of the four cases at $R_f^* \approx 1$ where Nu is minimum. For $R_f > 1$, Nu/Nu_0 starts to increase, suggesting a flow regime transition from buoyancy-dominated to shear-dominated convection. Results of $Nu(R_f)/Nu_0$ in figure 2 also suggest the flow transition is gradual for low Ra, whereas it becomes sharp with increasing Ra.

We show in figure 3 Nu as a function of Ra for various Re. In the TC-dominated regime, Nu changes slightly with varying Ra, and $Nu(Ra)$ collapses to the profile of pure RB convection with decreasing Re. The Ra range of the transitional regime (between the buoyancy- and shear-dominated regimes) is not as broad as that shown in plane Couette–RB flow (Blass *et al.* 2020), and we find the heat-transport scaling exponents exceed 0.3 for low $Re \leq 500$ and $Ra \leq 4 \times 10^7$. We infer that for low Ra it is the thermal plumes being swept away by the TVs that leads to the reduction of heat transport (see discussions in § 3.3). With increasing Ra, the plume structures become robust owing to strong buoyancy, and the sweeping away processes are weakening, leading to the rapid increasing in Nu, and the steep heat-transport scaling with a local exponent greater than 0.3.

3.2. *Angular velocity transport*

Annular velocity flux is another important transport quantity in the present system (Eckhardt *et al.* 2007). The angular velocity current is given as $J_\omega = [r^2\langle u_r u_\theta\rangle_{\theta z,t} - \nu r^3 \partial(\langle u_\theta\rangle_{\theta z,t}/r)/\partial r]$, with the first and second terms being the convective and diffusive fluxes, respectively. In circular Couette flow (CCF), the flow is laminar and has purely azimuthal velocity $u_\theta = Ar + B/r$, with $A = (r_2u_2 - r_1u_1)/(r_2^2 - r_1^2)$ and $B =$

https://doi.org/10.1017/jfm.2021.430 Published online by Cambridge University Press

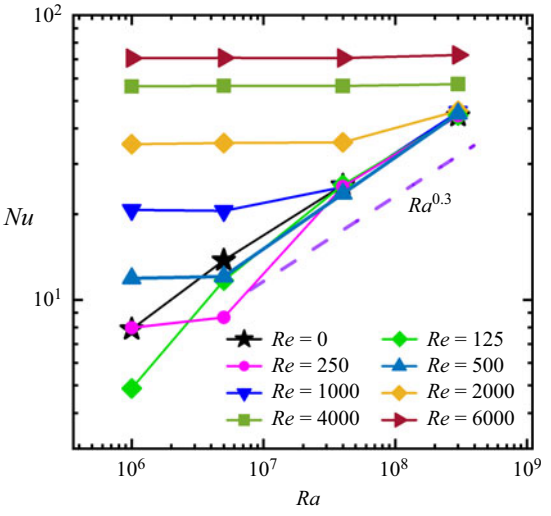


Figure 3. Plot of Nu as a function of Ra for various Re. The purple dashed line denotes a power-law scaling of $Ra^{0.3}$.

$(r_2^2 r_1 u_1 - r_2 r_1^2 u_2)/(r_2^2 - r_1^2)$. This flow produces an angular velocity current $J_{ccf} = 2\nu B$. By analogy with RB convection, the radial transport of angular velocity flux can be expressed by the ω-Nusselt number $Nu_\omega = J_\omega / J_{ccf}$ (Eckhardt *et al.* 2007; Ostilla-Mónico *et al.* 2014). In the axially periodical domain or very long cylinders, Nu_ω remains radially constant. However, owing to the braking effect of the fixed endwalls, Nu_ω decreases along the radial direction in our system. Here, we consider the flux at the inner cylinder

$$Nu_\omega = \frac{J_{\omega,r_1}}{J_{ccf}} = \frac{r_1^2 u_1}{2Bd} \frac{(2Re_\tau)^2}{Re}. \tag{3.1}$$

The dimensional torque at the inner cylinder reads

$$G_{r_1} = 2\pi r_1^3 h \rho \nu \frac{\partial}{\partial r} \left(\frac{\langle u_\theta \rangle_{\theta z,t}}{r} \right) = 2\pi r_1^2 h \frac{\rho \nu^2}{d^2} (2Re_\tau)^2, \tag{3.2}$$

where ρ is the fluid density. Following Lathrop's estimation (Lathrop *et al.* 1992*a*,*b*), we define the effective viscosity (owing to turbulent transport) as $\nu_t = G_{r_1}/(2\pi\rho u_1 r_1^2 h d^{-1})$. Thus, we obtain the equation of the dimensionless effective viscosity

$$\frac{\nu_t}{\nu} = \frac{(2Re_\tau)^2}{Re}. \tag{3.3}$$

Based on the friction Reynolds number, we find that ν_t/ν has the same scaling with Nu_ω,

$$Nu_\omega \sim \frac{\nu_t}{\nu} \sim \frac{Re_\tau^2}{Re} \sim Re^\gamma. \tag{3.4}$$

The results of ν_t/ν as a function of Re are shown in figure 4(*a*). We see that, when Ra is fixed, ν_t/ν decreases first to a minimum with increasing Re, after which the radial transport starts to increase. Further increasing the Reynolds number, all curves converge to a unifying transport scaling with $\gamma = 0.581 \pm 0.026$ for $Re > 2000$ (see the compensated

https://doi.org/10.1017/jfm.2021.430 Published online by Cambridge University Press

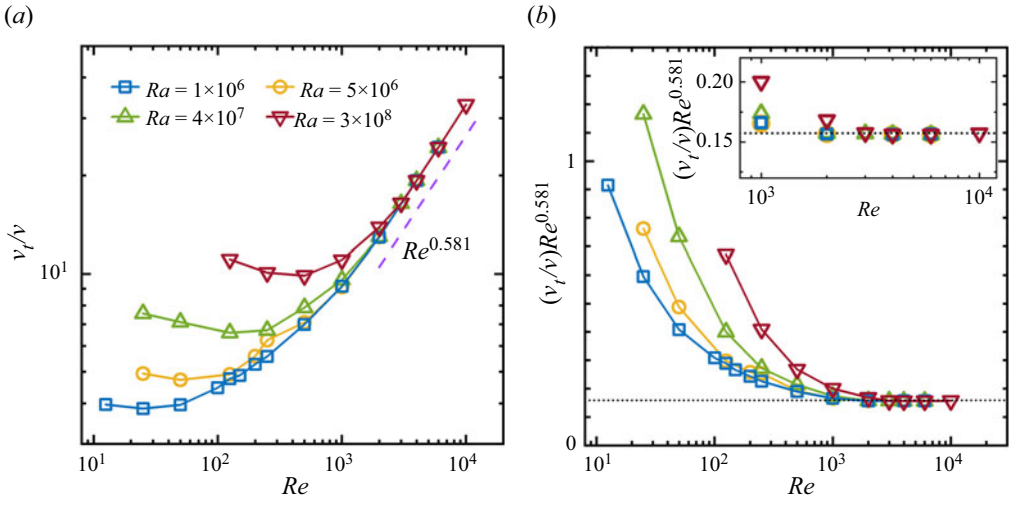


Figure 4. (*a*) Dimensionless effective viscosity ν_t/ν as a function of Re. The purple dashed line denotes a power-law scaling of $Re^{0.581}$. (*b*) Compensated ν_t/ν as a function of Re. The dotted line is the auxiliary line for $(\nu_t/\nu)/Re^{0.581} = 0.156$. Inset: an expanded view of the data in the range of $1000 \leq Re \leq 10\,000$.

plot in figure 4*b*). This scaling exponent is similar to that observed in TC flows by Merbold, Brauckmann & Egbers (2013) at the same Re range and with the same radius ratio. Interestingly, here we find that the both scalings of axial heat and radial angular velocity transport coincide approximately with each other for $2000 < Re \leq 10\,000$.

For the lowest Re for each Ra, we find ν_t/ν increases monotonically with increasing Ra, indicating that the energetic structures in RB-type convection could contribute more momentum to the radial transport process (see detailed discussions about the contribution of RB flow to the radial transport in Appendix C). It is the structures of thermal plumes and LSC that govern the heat and momentum transport processes in pure RB convection ($Re = 0$). When weak rotations are present, we suggest that with increasing Ra these structures become more vigorous and provide the system with more efficient radial angular velocity transport.

3.3. *Flow morphology*

To gain some insights into the transitional behaviour of $Nu(Re)$ and its pronounced enhancement in the shear-dominated regime, we visualise the flow fields of the instantaneous temperature $T(R, Z)$ and velocity $\boldsymbol{U}(R, Z)$ in the vertical cross-sections in figure 5. The four panels in figures 5(*a*)–5(*d*) present results for $Ra = 10^6$ with Re increasing from left to right. Figure 5(*a*) shows that for low $Ra = 10^6$ and $Re = 12.5$, the flow field and local heat transfer are dominated by large-scale vertical plumes emanating from TBLs. We see that for this Re the imposed rotation is too weak to influence the flow organisation in the bulk, thus the main flow features are analogous to those in non-rotating RB convection. For $Re = 50$, figure 5(*b*) shows that the thermal plumes are organised into TVs. We find in this state a reduction of 30 % in Nu as shown in figure 1. In our system with finite axial length, the strong inward shears of TVs at the endwalls disperse the thermal plumes, and prevent them from traversing through the fluid layer, leading to a prominent reduction of heat transfer. A similar mechanism of heat-transfer reduction is also found in

https://doi.org/10.1017/jfm.2021.430 Published online by Cambridge University Press

other shear convection systems (Scagliarini, Gylfason & Toschi 2014; Blass *et al.* 2020), where the flow sweeps away the thermal plumes and inhibits the turbulent heat transfer.

When Nu reaches a minimum at $Re = 125$ ($R_f = 1$, figure 5*c*), the flow field is dominated by two nearly symmetric TVs which occupy the entire domain. Owing to the prominent intra-vortex mixing (Kataoka & Takigawa 1981; Akonur & Lueptow 2002, 2003), we find that the axial heat transport between adjacent TVs is severely restricted at this configuration.

Further increasing Re, results in the emergence of chaotic flow ($Re = 1000$, figure 5*d*) promotes large heat and mass exchanges between vortices. This could be explained by the further development of TV flow towards a more disordered state (Andereck *et al.* 1986), providing a higher axial mixing efficiency over the stacked vortices, namely, in the form of inter-vortex mixing (Kataoka & Takigawa 1981; Akonur & Lueptow 2002, 2003).

Figure 5(*e–h*) present the evolution of flow structures with increasing Re at $Ra = 3 \times 10^8$. At low $Re = 125$ and 500, the plumes are rising up (falling down) from the bottom (top) boundary layers. Since the plumes become robust in the presence of strong buoyancy (high Ra), they are hardly disturbed by rolls, unlike the flow of figure 5(*b*) in which the plumes are much more easily entrained. When $Re = 1000$, we observe that these plumes become distorted by the shear flows and evolve into rolls (figure 5*g*). In this high Ra turbulence, the bulk flows consist of rich small-scale structures (e.g. plumes and vortices) which in general cannot be degraded by the imposed shear, preventing the formation of laminar TVs. The robust thermal plumes emanating from the boundary layers may sustain the global heat transfer at a high level. For this reason, we find with increasing Re only a weak reduction of Nu for $Ra = 4 \times 10^7$, and even no reduction of Nu for $Ra = 3 \times 10^8$ in figure 1. Further increasing Re, the flow system jumps over the state of laminar TV flow characterised by the regular two-vortex structure (figure 5*c*), and directly enters the TTVF at $Re = 4000$ (figure 5*h*).

As demonstrated in figures 1, 2 and 4, with high enough Re the convection system enters a shear-dominated regime where heat and angular velocity transport are highly intensified and governed by a power-law scaling of approximately $Re^{0.58}$ irrespective of Ra for $Re > 2000$. To further characterise this flow state, we show in figure 6 representatively instantaneous temperature and mean velocity fields. Here, for different Ra, they promote very similar flow structures typified by small-scale eddies (figure 6*a–d*), and the common structures of TTVF are raised and recognised by the two-roll structures in the mean flow field (figure 6*e–h*). In this turbulent state, the transport of heat and angular velocity fluxes is independent of Ra and completely governed by turbulent TVs.

We suggest that the comparable transport of heat and angular momentum can be understood through the hypothesis that in turbulent TC flow the axial transport for passive scalar should share the same scaling behaviours as the radial transport of angular momentum (Lathrop *et al.* 1992*a*), based on the Reynolds analogy (Kays & Crawford 1980). The underlying physics of the analogous scaling forms of heat and angular momentum transport remains to be further explored. Moreover, in the present small-Γ geometry where the endwall flows inevitably influence both the heat and angular momentum transport, we find their scaling exponents remain still comparable. How the endwall effects modify the scaling of turbulent transport is a challenge for future studies.

Visualisation of the temperature fields (figure 6*a–d*) illustrates clearly how heat is transported axially. The inward flows induced by the pressure imbalance at the endwalls sweep away TBLs. Consequently, the hot and cold fluids therein are driven away rapidly and feed the axial flows along the inner wall into the bulk. The outward jets usually

https://doi.org/10.1017/jfm.2021.430 Published online by Cambridge University Press

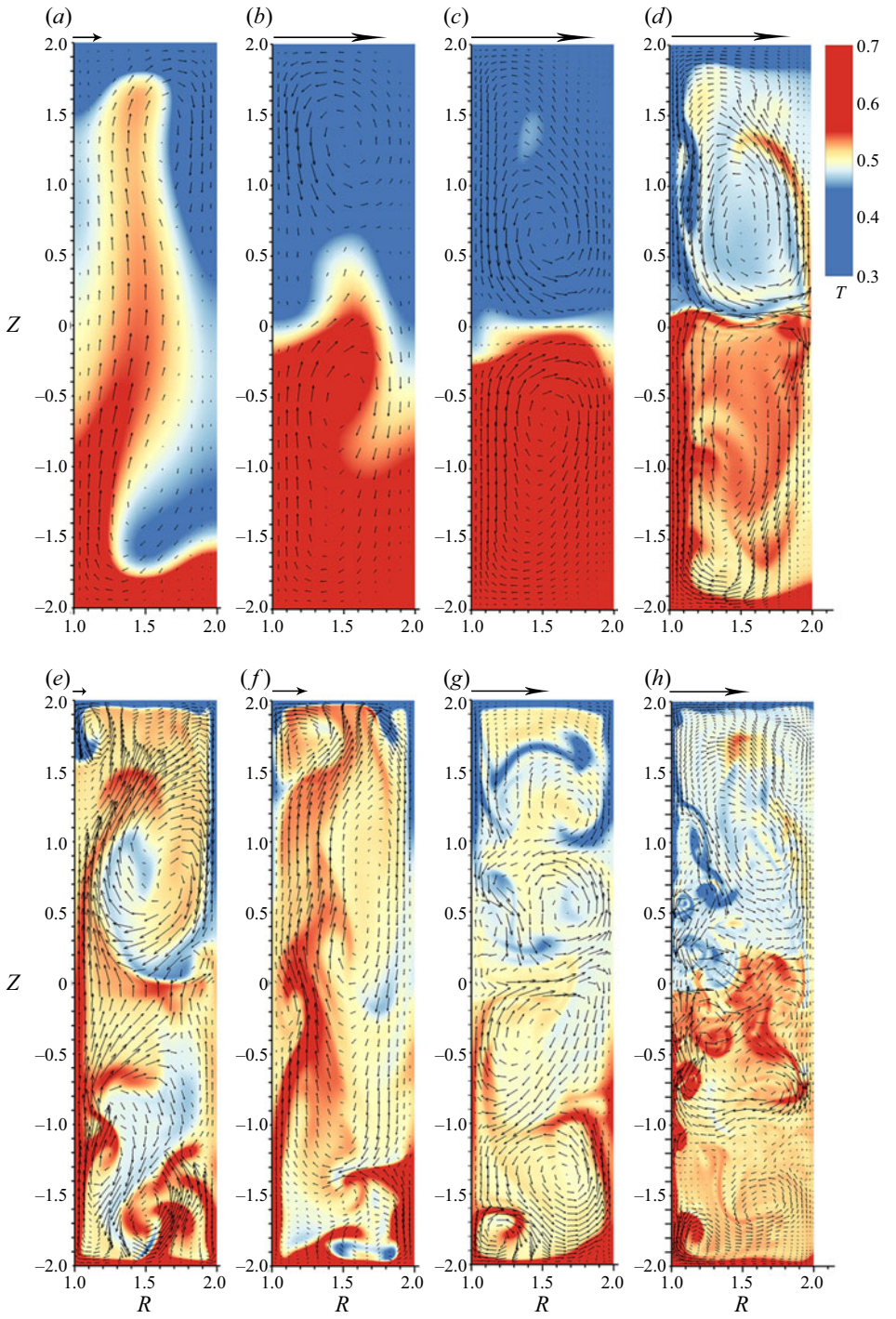


Figure 5. Distributions of instantaneous temperature and velocity fields in a meridional plane. (*a–d*) Results for $Ra = 10^6$ and Re = 12.5, 50, 125 and 1000, respectively. (*e–h*) Results for $Ra = 3 \times 10^8$ and Re = 125, 500, 1000 and 4000, respectively. In each panel, the left and right sides denote the inner and outer cylinders. To facilitate visualisation, the arrow lengths are plotted in various scales in different panels, with the arrows on the top indicating the velocity scale of the inner cylinder. See Supplementary Movies 1–4 available at https://doi.org/10.1017/jfm.2021.430 for the three-dimensional temperature fields corresponding to panels (*e–h*).

https://doi.org/10.1017/jfm.2021.430 Published online by Cambridge University Press

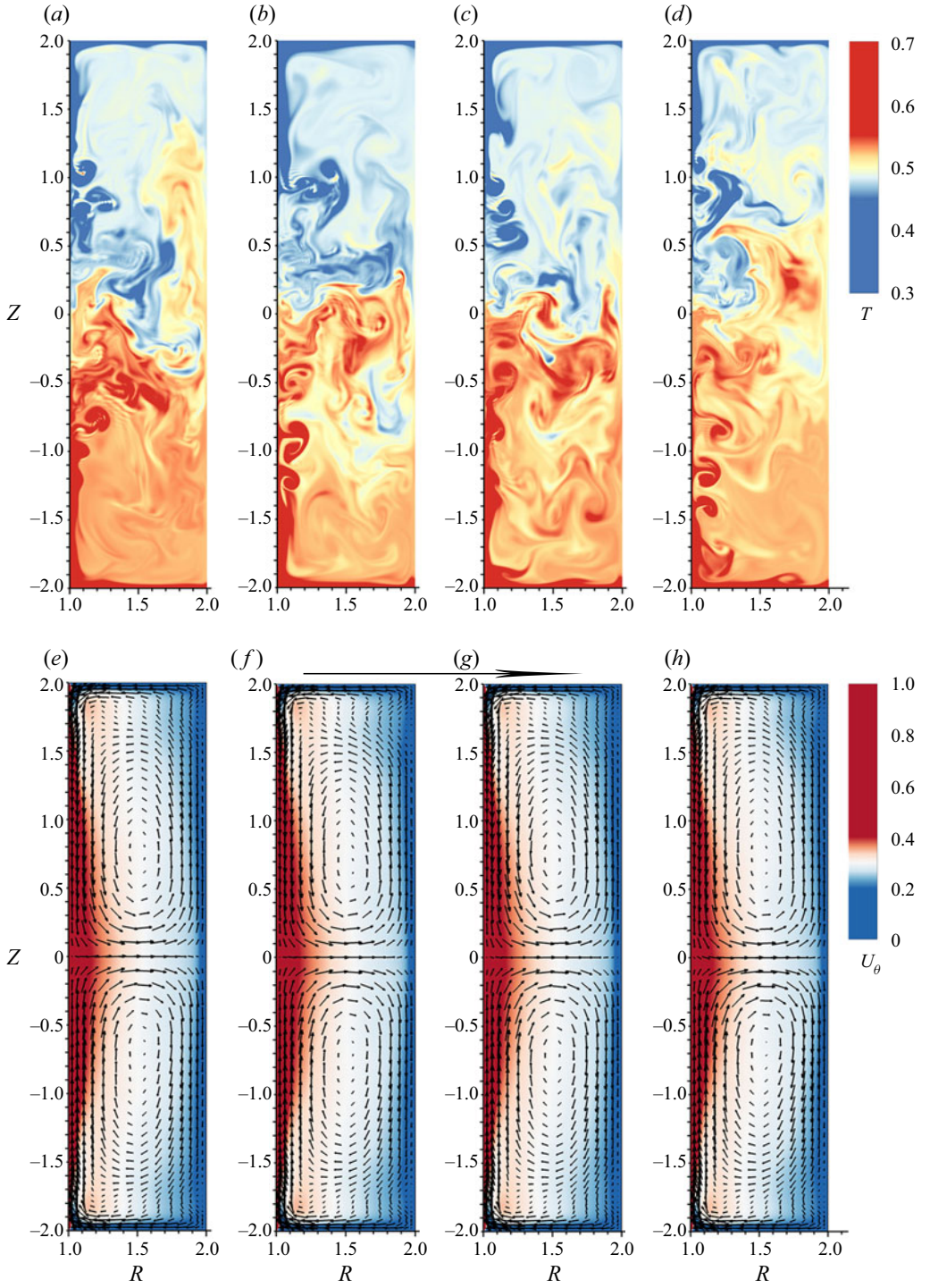


Figure 6. Distributions of the instantaneous temperature $T(R, Z)$ (*a–d*) and the time-averaged azimuthal velocity $U_\theta(R, Z)$ (*e–h*) with $Ra = 10^6$ (*a*,*e*), 5×10^6 (*b*,*f*), 4×10^7 (*c*,*g*) and 3×10^8 (*d*,*h*) for $Re = 6000$. The arrow on the top indicates the velocity scale of the inner cylinder.

https://doi.org/10.1017/jfm.2021.430 Published online by Cambridge University Press

play important roles in the radial transport of angular momentum (Van Der Veen *et al.* 2016), and here, they act on enhancing the axial mixing of the hot and cold fluids, accompanying the π-shaped Görtler vortices (Dong 2007). Finally, the mixed fluids follow the upward/downward flows of rolls along the outer cylinders, returning to TBLs. This resembles a high efficiency thermal pump providing the steep heat-transfer scaling of our cases.

3.4. *Regimes transition*

We have shown the different properties of heat transport and flow structures in both the RB- and TC-dominated regimes. In general, the main flow structures in RB and TC flows are characterised by small-scale plumes and large-scale vortices, respectively. In the following analysis, we decompose the flow field into mean TV flow (*m*TVF) and the fluctuations (Bilson & Bremhorst 2007; Froitzheim *et al.* 2019), i.e. $\boldsymbol{U} = \boldsymbol{U}' + \langle \boldsymbol{U} \rangle_{\theta,t}$ and $T = T' + \langle T \rangle_{\theta,t}$, in order to identify their individual contributions to the global heat transport. The convective Nusselt number reads $Nu_c = Nu - 1 = Nu_{TV} + Nu_{fl}$, with its contribution from large-scale structures of the *m*TVF, namely, $Nu_{TV} = \sqrt{Ra\,Pr}\langle \langle U_z \rangle_{\theta,t} \langle T - T_0 \rangle_{\theta,t} \rangle$, and the contribution from turbulent fluctuations, $Nu_{fl} = \sqrt{Ra\,Pr}\langle U_z' T' \rangle$, where T_0 is the mean fluid temperature.

Figure 7(*a–d*) show the ratios Nu_{TV}/Nu and Nu_{fl}/Nu as functions of Re. In the buoyancy-dominated regime, we see that heat transport through turbulent fluctuations is dominant. For $Ra = 10^6$, Nu_{TV}/Nu increases while Nu_{fl}/Nu decreases gradually with increasing Re. Curves of $Nu_{TV}(Re)$ and $Nu_{fl}(Re)$ intersect at $Re^* \approx 100$ indicating a smooth transition. However, at larger $Ra \geq 5 \times 10^6$, Nu_{TV}/Nu decreases slightly and then starts to increase steeply, while Nu_{fl}/Nu undergoes variations in the opposite direction. They meet and cross sharply at a transitional point Re^* which increases with increasing Ra. These results indicate the fading away of thermal plumes in the RB-type convection and newly forming TVs in the TC-type turbulence. The Ra-dependence of Re^* suggests that stronger buoyancy delays transition. Furthermore, the flow transition changes from smooth at low Ra to sharp at high Ra, which is consistent with the observation in figure 2. Interestingly, we find that for $Ra \leq 5 \times 10^6$, the global heat transfer consists mostly of Nu_{TV} in the range of $250 \leq Re \leq 500$, where the main flow structures are laminar TVs as shown in figure 5(*c*). For $Ra \geq 4 \times 10^7$, we have seen in figure 5 that with increasing Re the RB-type flows evolve into TTVF. For this reason we see that in the TC-dominated convection the percentage of heat transport by turbulent fluctuations (Nu_{fl}) remains at 30 %. For the range of largest $Re > 2000$, the four sets of data curves at various Ra converge to a unique state with $Nu_{TV}/Nu \approx 0.7$ and $Nu_{fl}/Nu \approx 0.3$.

Data curves of $Nu_{TV}(Re)$ and $Nu_{fl}(Re)$ in figure 7(*a–d*) exhibit a genetic crossover from RB-type convection to another type of convection dominated by the turbulent TC flow, although the transitional value Re^* depends on Ra. To examine the universal transitional behaviours, we present in figure 7(*e*) the results of Nu_{TV}/Nu and Nu_{fl}/Nu as functions of R_f. Notably, one sees that the crossovers of both $Nu_{TV}/Nu(R_f)$ and $Nu_{fl}/Nu(R_f)$ occur at the same transitional regime with $R_f \approx 1$. The shaded area denotes the transition region of the minimum heat transport $Nu_m(R_f^*)$ as plotted in figure 2. The data thus suggest that in the flow regime where the buoyancy is dominant ($R_f < 1$), the temporal fluctuations of the flows associated with the buoyancy-driven thermal plumes play the leading role in determining Nu. Whereas in the shear-dominated regime ($R_f > 1$), the large-scale mean flows, i.e. the turbulent TVs, provide the large contribution to the global heat transport.

https://doi.org/10.1017/jfm.2021.430 Published online by Cambridge University Press

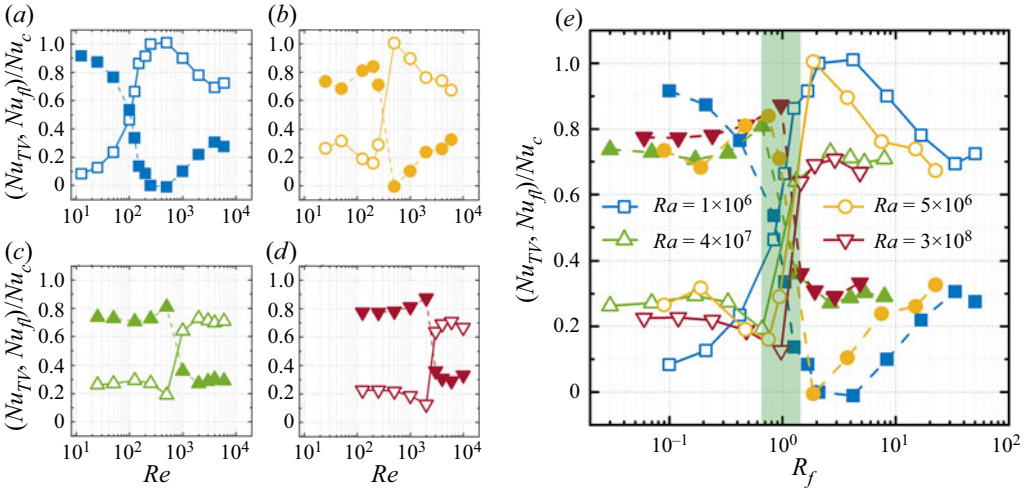


Figure 7. Heat transport by the mean TV flow Nu_{TV} and by turbulent fluctuations Nu_{fl}, as functions of Re at (*a*) $Ra = 10^6$, (*b*) 5×10^6, (*c*) 4×10^7 and (*d*) 3×10^8. (*e*) Nu_{TV} and Nu_{fl} as functions of R_f. Open symbols: data of Nu_{TV}. Solid symbols: data for Nu_{fl}. The shaded area indicates the transitional region.

In the balance of buoyancy and shear effects ($R_f \approx 1$) we observe the crossovers of these two regimes coinciding with the transitional value of the global heat transport as shown in figure 2.

We suggest that it is the force balance between inertia and buoyancy that governs the transition from RB- to TC-type convection. We compare in figure 8 the volume- and time-averaged root mean square (r.m.s.) forces of inertia $F_i = \sqrt{\langle[(\boldsymbol{U}\cdot\nabla)\boldsymbol{U}]^2\rangle_{V,t}}$, viscous $F_v = \sqrt{\langle(Pr^{0.5}Ra^{-0.5}\nabla^2\boldsymbol{U})^2\rangle_{V,t}}$ and buoyancy $F_b = \sqrt{\langle(Te_z)^2\rangle_{V,t}}$ in (2.1), as functions of R_f for $Ra = 4 \times 10^7$ and 3×10^8. With increasing R_f, although the buoyancy remains approximately constant ($F_b \approx 0.5$), both F_i and F_v increase from the buoyancy-dominated regime ($R_f \ll 1$) where they are one order of magnitude below F_b. F_i and F_v cross the value of F_b in the vicinity of $R_f = 1$, i.e. the transitional region shown in figures 2 and 7(*e*). In the shear-dominated regime with $R_f \gg 1$, we see that F_i exceeds F_v and both dominate F_b, indicating that the flows in this regime are in a highly turbulent state and that buoyancy becomes negligible. Similar R_f-dependence of the various force components are observed for all Ra studied. And we conclude that it is the interior force balance that provides a quantitative constraint for determining the flow-regime transition.

4. Conclusion and discussion

In the present study, we investigate the effects of TC flow on the heat transport by thermal convection in an annular domain driven by an axially-imposed temperature gradient. For weak rotations ($R_f < 1$), the fluid system inherits the main flow features of ordinary RB convection with thermal plumes emanating from the TBLs. In this buoyancy-dominated regime, the thermal plumes are more easily dispersed by shear flows if Ra is low ($Ra \leq 5 \times 10^6$), leading to a reduction of the global heat transport. For high $Ra \geq 4 \times 10^7$, the vigorous thermal plumes maintain their vertical motion under the strong buoyancy and traverse deeply into the bulk fluid, thus Nu becomes independent of the applied rotations. In the shear-dominated regime ($R_f > 1$), the flow features and heat transport are dominated by TVs. The transition between the RB-type convection to the TC-type occurs at a critical

https://doi.org/10.1017/jfm.2021.430 Published online by Cambridge University Press

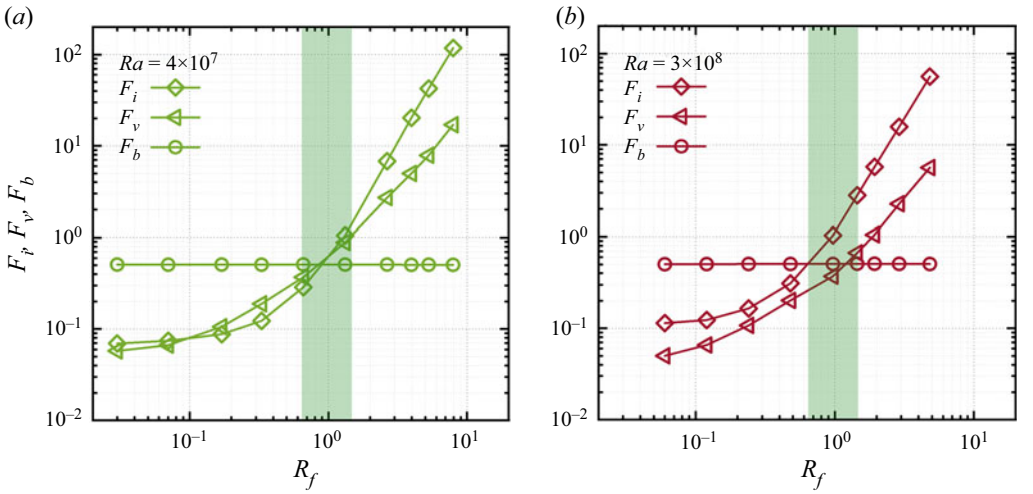


Figure 8. The r.m.s. forces as functions of R_f for (*a*) $Ra = 4 \times 10^7$ and (*b*) $Ra = 3 \times 10^8$. Here F_i, F_v and F_b denote inertia, viscous and buoyant forces, respectively. The shaded area indicates the transitional region.

value $R_f \approx 1$. We report that the main heat carriers change from small-scale thermal plumes to large-scale *m*TVF. Meanwhile, the flows evolve from the state where the fluid motion is dominated by the buoyancy to another state by the inertia force. The transition is found to be gradual for low *Ra* but becomes sharp at high *Ra*.

In our study, the TVs are introduced by immersing the rotating inner cylinder into the flow field. In the shear-dominated flow regime where these turbulent structures are prominent, a new power-law scaling of the effective heat transport ($Nu \sim Re^{0.578\pm0.018}$) is found for $2000 < Re \leq 10\,000$, and it shows the strong similarity with the scaling of the angular velocity flux ($Nu_\omega \sim Re^{0.581\pm0.026}$). This result is consistent with the early work of Lathrop *et al.* (1992*a*). We infer that in this turbulent state it is the coherent structures in the form of turbulent TVs that provide the efficient mechanism for both the axial heat transport and radial momentum transport simultaneously.

The analogy between heat and momentum transport in rotating flow has been derived by Bradshaw (1969), and one may think that our system should relate to this analogy. However, our axial heat transport is perpendicular to the momentum transfer direction, differing from the simplified model of wall-normal direction in Bradshaw's analogy, which means that, in our system the meridional advection governs both transport processes. Hence, we cannot make a direct connection of the present cases with this analogy. Further work and analysis of the two-dimensional turbulent-kinetic-energy budgets are necessary.

By controlling the rotating conditions, the TC flow may bifurcate to various cell modes and have different transport behaviours (Wen *et al.* 2020). In our study, in addition to the commonly observed two-cell mode, convection in a four-cell mode can be seen occasionally when diverse initial conditions are used. In the four-cell convection mode we find the main results discussed heretofore unchanged.

This study, where $Re = 10^4$ is the largest value used, is still in the classical regime of turbulent TC flow, thus our obtained scaling exponent does not exceed the well-accepted value ($\leq 2/3$) for the angular velocity flux in the classical turbulent regime (Grossmann *et al.* 2016). Extending the present studies to the ultimate turbulent regime ($Re > 10^5$) remains an interesting challenge. Furthermore, the effects of the radius ratio, the axial

https://doi.org/10.1017/jfm.2021.430 Published online by Cambridge University Press

domain boundaries (the endwalls), and also the Prandtl number are intriguing subjects for future studies.

Supplementary movies. Supplementary movies are available at https://doi.org/10.1017/jfm.2021.430.

Funding. This work was supported by the National Natural Science Foundation of China under grant numbers 11902224, 51976021 and 11772235, and the China Postdoctoral Science Foundation (No.2019M651572).

Declaration of Interests. The authors report no conflict of interest.

Author ORCIDs.
J.-Q. Zhong https://orcid.org/0000-0001-8368-2120.

Appendix A. Numerical details

The results of the grid sensitivity study are listed in table 1. Tables 2, 3, 4 and 5 list the main results for $Ra = 10^6$, 5×10^6, 4×10^7 and 3×10^8 respectively. In the tables, $N_\theta \times N_z \times N_r$ are the numbers of grid points in three directions; σ_h is the time convergence of the Nusselt numbers averaged over the whole and the last half simulation periods; σ_{ϵ_T} is the relative error measured by Nu and the thermal dissipation rate; $L_{max}/(\langle\lambda_k\rangle, \langle\lambda_b\rangle)$ are the maximal grid spacings compared with the Kolmogrov and Batchelor scales; Δr^+_{min}, Δr^+_{max} are the minimal and maximal grid sizes in wall units; t_{u_1} is the averaging time normalised by the large-eddy turnover time unit d/u_1; and t_{u_f} is the averaging time normalised by the free fall time unit h/u_f.

Appendix B. Validation of the centrifugal buoyancy

The additional simulations considering the effect of centrifugal buoyancy are performed for $Ra = 10^6$ and 3×10^8, by using the realistic condition with $\Delta = 10$ K and $\beta = 0.00038$ K^{-1}. The main results are listed in table 6. As shown in figure 9, for both the lowest and highest Ra considered here, we find that including the centrifugal buoyancy does not change the results of heat transport.

Appendix C. Flows as passive scalar

The additional simulations for the passive scalar in TC systems are performed at $Ra = 3 \times 10^8$, where the temperature is treated as a passive scalar by removing the buoyancy term from the momentum equation (2.1) numerically. The main results are listed in table 7 and shown in figures 10(a) and 10(b) respectively.

We find that, both Nu and ν_t/ν in the flows of the active scalar diverge from those of the passive scalar at low Re, and then they converge gradually with the increasing Re. Beyond $Re > 2000$, the curves of the passive scalar coincide with those of the active scalar, indicating that the temperature in the TC-dominated regime acts like a passive scalar.

Furthermore, in figure 10(b), in the flows where the temperature is treated as a passive scalar, ν_t/ν increases monotonically with increasing Re, while it decreases firstly at low Re for the active-scalar cases. We observe that in our system, the coherent structures in the RB-type convection could provide higher radial transport in the lowest Re flows. And these structures are destroyed with increasing Re, resulting in the local minimum of ν_t/ν for $Re = 500$. Further increasing Re, ν_t/ν starts to increase and then, thanks to the formation of TVs, the curve coincides with the curve of the passive scalar (pure TC flow) for $Re > 2000$, when the flows are dominated by turbulent TVs completely.

https://doi.org/10.1017/jfm.2021.430 Published online by Cambridge University Press

Ra	Re	R_f	$N_\theta \times N_z \times N_r$	Nu	σ_h	σ_{ϵ_T}	Re_τ	$\frac{L_{max}}{\langle\lambda_k\rangle,\langle\lambda_b\rangle}$	$\Delta r^+_{min}, \Delta r^+_{max}$	t_{u_1}, t_{u_f}
1×10^6	0	0	$64 \times 65 \times 25$	7.88	1.00	0.98	—	0.57, 1.19	—,—	—, 195.63
1×10^6	12.5	0.10	$64 \times 65 \times 25$	7.41	1.00	0.99	3.52	0.61, 1.27	0.14, 0.42	89.57, 214.00
1×10^6	25	0.21	$64 \times 65 \times 25$	6.32	0.99	0.99	4.91	0.68, 1.43	0.20, 0.59	211.17, 252.25
1×10^6	50	0.42	$96 \times 97 \times 33$	5.13	0.98	0.99	7.03	0.89, 1.86	0.28, 0.84	199.24, 119.00
1×10^6	100	0.84	$96 \times 97 \times 33$	5.07	1.00	0.99	10.57	0.88, 1.84	0.31, 0.95	386.97, 115.56
1×10^6	125	1.05	$96 \times 97 \times 33$	4.88	1.00	0.97	12.20	0.99, 2.08	0.36, 1.10	359.71, 85.94
1×10^6	150	1.26	$128 \times 129 \times 33$	6.48	1.00	0.97	13.52	1.09, 2.29	0.39, 1.21	253.02, 50.38
1×10^6	200	1.67	$128 \times 129 \times 33$	7.46	1.00	0.98	16.24	1.07, 2.23	0.47, 1.46	572.18, 85.44
1×10^6	250	2.09	$128 \times 129 \times 33$	7.97	1.00	0.96	18.66	1.21, 2.53	0.55, 1.68	482.92, 57.69
1×10^6	500	4.19	$192 \times 193 \times 49$	11.90	1.00	0.97	29.56	1.20, 2.51	0.56, 1.77	513.58, 30.68
1×10^6	1000	8.37	$256 \times 257 \times 65$	20.71	0.99	0.99	47.86	1.44, 3.01	0.53, 2.36	363.95, 10.87
1×10^6	2000	16.74	$384 \times 385 \times 97$	35.23	1.00	0.98	80.36	1.47, 3.08	0.59, 2.65	305.39, 4.56
1×10^6	4000	33.49	$512 \times 513 \times 129$	56.27	1.00	0.97	138.84	1.72, 3.59	0.75, 3.43	469.47, 3.51
1×10^6	6000	50.23	$768 \times 721 \times 181$	70.67	1.00	0.99	191.44	1.55, 3.24	0.74, 3.36	253.05, 1.26

Table 2. Summary of results at $Ra = 1 \times 10^6$.

Ra	Re	R_f	$N_\theta \times N_z \times N_r$	Nu	σ_h	σ_{ϵ_T}	Re_τ	$\frac{L_{max}}{\langle\lambda_k\rangle,\langle\lambda_b\rangle}$	$\Delta r^+_{min}, \Delta r^+_{max}$	t_{u_1}, t_{u_f}
5×10^6	0	0	$96 \times 97 \times 29$	13.77	0.99	0.99	—	0.72, 1.52	—, —	—, 246.25
5×10^6	25	0.09	$96 \times 97 \times 29$	13.56	0.99	0.99	5.55	0.75, 1.57	0.19, 0.57	96.68, 258.25
5×10^6	50	0.19	$96 \times 97 \times 29$	13.46	1.00	0.99	7.68	0.82, 1.72	0.26, 0.79	194.12, 259.25
5×10^6	125	0.47	$96 \times 97 \times 29$	11.69	0.98	0.99	12.38	1.09, 2.29	0.42, 1.27	476.40, 254.50
5×10^6	200	0.75	$128 \times 129 \times 33$	10.08	0.98	0.98	16.71	1.09, 2.29	0.49, 1.50	680.43, 227.19
5×10^6	250	0.94	$192 \times 161 \times 41$	8.67	0.99	0.98	19.77	0.94, 1.96	0.46, 1.42	2161.81, 577.44
5×10^6	500	1.87	$192 \times 193 \times 49$	12.07	1.00	0.97	29.79	1.20, 2.52	0.57, 1.79	657.04, 87.75
5×10^6	1000	3.74	$256 \times 257 \times 65$	20.53	1.00	0.99	47.73	1.35, 2.83	0.68, 2.15	450.19, 30.06
5×10^6	2000	7.49	$384 \times 385 \times 97$	35.54	1.00	0.97	80.38	1.47, 3.08	0.59, 2.65	291.84, 9.74
5×10^6	4000	14.98	$512 \times 513 \times 129$	56.47	1.00	1.00	138.94	1.72, 3.59	0.76, 3.43	419.90, 7.01
5×10^6	6000	22.46	$768 \times 721 \times 181$	70.88	0.99	0.99	191.21	1.55, 3.24	0.74, 3.36	276.18, 3.07

Table 3. Summary of results at $Ra = 5 \times 10^6$.

Ra	Re	R_f	$N_\theta \times N_z \times N_r$	Nu	σ_h	σ_{ϵ_T}	Re_τ	$\frac{L_{max}}{\langle\lambda_k\rangle,\langle\lambda_b\rangle}$	$\Delta r^+_{min}, \Delta r^+_{max}$	t_{u_1}, t_{u_f}
4×10^7	0	0	$192 \times 193 \times 49$	25.29	1.00	0.99	—	0.64, 1.34	—, —	—, 488.00
4×10^7	25	0.03	$192 \times 193 \times 49$	25.34	0.98	0.99	6.87	0.76, 1.58	0.13, 0.41	36.55, 276.13
4×10^7	50	0.07	$192 \times 193 \times 49$	25.35	1.00	0.99	9.43	0.79, 1.65	0.18, 0.57	39.74, 150.13
4×10^7	125	0.17	$192 \times 193 \times 49$	25.35	1.00	0.99	14.36	0.84, 1.77	0.27, 0.86	104.90, 158.50
4×10^7	250	0.33	$192 \times 193 \times 49$	25.00	1.00	0.99	20.48	0.98, 2.06	0.39, 1.23	398.08, 300.75
4×10^7	500	0.66	$192 \times 193 \times 49$	23.60	0.98	0.99	31.39	1.31, 2.75	0.60, 1.88	432.17, 163.25
4×10^7	1000	1.32	$256 \times 257 \times 65$	24.92	0.99	0.98	48.94	1.46, 3.06	0.54, 2.42	405.83, 76.65
4×10^7	2000	2.65	$384 \times 385 \times 97$	35.77	1.00	0.98	80.53	1.47, 3.09	0.59, 2.65	298.35, 28.18
4×10^7	3000	3.97	$384 \times 449 \times 113$	47.08	1.00	0.97	110.88	1.72, 3.60	0.69, 3.13	366.12, 23.05
4×10^7	4000	5.29	$512 \times 513 \times 129$	56.40	0.99	0.97	138.93	1.72, 3.59	0.76, 3.43	469.52, 22.17
4×10^7	6000	7.94	$768 \times 721 \times 181$	70.76	0.97	0.99	191.13	1.55, 3.24	0.74, 3.36	264.66, 8.33

Table 4. Summary of results at $Ra = 4 \times 10^7$.

https://doi.org/10.1017/jfm.2021.430 Published online by Cambridge University Press

Ra	Re	R_f	$N_\theta \times N_z \times N_r$	Nu	σ_h	σ_{ϵ_T}	Re_τ	$\frac{L_{max}}{\langle\lambda_k\rangle,\langle\lambda_b\rangle}$	$\Delta r^+_{min}, \Delta r^+_{max}$	t_{u_1}, t_{u_f}
3×10^8	0	0	$384 \times 385 \times 97$	44.28	1.00	1.00	—	0.62, 1.30	—, —	—, 684.80
3×10^8	125	0.06	$384 \times 385 \times 97$	44.42	0.99	0.99	18.61	0.75, 1.57	0.17, 0.56	36.66, 151.69
3×10^8	250	0.12	$384 \times 385 \times 97$	44.40	1.00	0.99	25.11	0.77, 1.62	0.23, 0.75	78.63, 162.69
3×10^8	500	0.24	$384 \times 385 \times 97$	45.10	0.99	0.99	35.13	0.85, 1.77	0.33, 1.05	158.59, 164.06
3×10^8	1000	0.48	$384 \times 385 \times 97$	45.73	1.00	0.99	52.53	1.05, 2.20	0.49, 1.57	386.90, 200.13
3×10^8	2000	0.97	$384 \times 385 \times 97$	46.14	0.99	0.98	83.30	1.52, 3.18	0.61, 2.74	548.33, 141.81
3×10^8	3000	1.45	$384 \times 449 \times 113$	48.30	0.99	0.97	111.04	1.73, 3.63	0.69, 3.13	398.45, 68.70
3×10^8	4000	1.93	$512 \times 513 \times 129$	57.29	0.99	0.97	138.84	1.72, 3.60	0.76, 3.43	437.70, 56.60
3×10^8	6000	2.90	$768 \times 721 \times 181$	72.52	1.00	0.97	191.21	1.55, 3.25	0.74, 0.73	291.97, 25.17
3×10^8	10 000	4.83	$1024 \times 1001 \times 251$	96.86	0.97	0.98	287.38	1.57, 3.29	0.79, 3.64	123.63, 6.40

Table 5. Summary of results at $Ra = 3 \times 10^8$.

Ra	Re	R_f	$N_\theta \times N_z \times N_r$	Nu	σ_h	σ_{ϵ_T}	Re_τ	$\frac{L_{max}}{\langle\lambda_k\rangle,\langle\lambda_b\rangle}$	$\Delta r^+_{min}, \Delta r^+_{max}$	t_{u_1}, t_{u_f}
1×10^6	125	1.05	$96 \times 97 \times 33$	4.89	1.00	0.97	12.20	0.99, 2.08	0.36, 1.10	1220.91, 291.69
1×10^6	250	2.09	$128 \times 129 \times 33$	7.97	1.00	0.96	18.66	1.21, 2.53	0.55, 1.68	1353.55, 161.69
1×10^6	500	4.19	$192 \times 193 \times 49$	11.90	1.00	0.97	29.55	1.20, 2.51	0.56, 1.77	275.84, 16.48
1×10^6	1000	8.37	$256 \times 257 \times 65$	20.69	1.00	0.98	47.87	1.44, 3.01	0.53, 2.36	304.51, 9.09
1×10^6	2000	16.74	$384 \times 385 \times 97$	35.29	1.00	0.98	80.45	1.47, 3.08	0.59, 2.65	663.26, 9.90
1×10^6	4000	33.49	$512 \times 513 \times 129$	55.99	0.99	0.97	138.94	1.72, 3.59	0.76, 3.43	434.31, 3.24
1×10^6	6000	50.23	$768 \times 721 \times 181$	71.49	0.99	0.98	191.25	1.55, 3.25	0.74, 3.36	252.15, 1.26
3×10^8	125	0.06	$384 \times 385 \times 97$	44.72	0.10	0.99	18.65	0.75, 1.58	0.17, 0.56	36.43, 150.75
3×10^8	250	0.12	$384 \times 385 \times 97$	44.49	0.99	0.99	24.98	0.77, 1.62	0.23, 0.75	77.42, 160.19
3×10^8	500	0.24	$384 \times 385 \times 97$	44.88	1.00	0.99	34.98	0.85, 1.77	0.33, 1.05	124.75, 129.05
3×10^8	1000	0.48	$384 \times 385 \times 97$	45.55	0.99	0.99	52.58	1.05, 2.20	0.49, 1.58	249.78, 129.20
3×10^8	2000	0.97	$384 \times 385 \times 97$	46.11	0.98	0.97	83.43	1.52, 3.19	0.61, 2.75	776.46, 200.81
3×10^8	3000	1.45	$384 \times 449 \times 113$	47.13	0.97	1.00	111.26	1.73, 3.63	0.69, 3.14	515.68, 88.91
3×10^8	4000	1.93	$512 \times 513 \times 129$	57.03	1.00	0.97	138.62	1.72, 3.60	0.75, 3.42	319.57, 41.33

Table 6. Summary of results with centrifugal buoyancy at $Ra = 1 \times 10^6$ and 3×10^8.

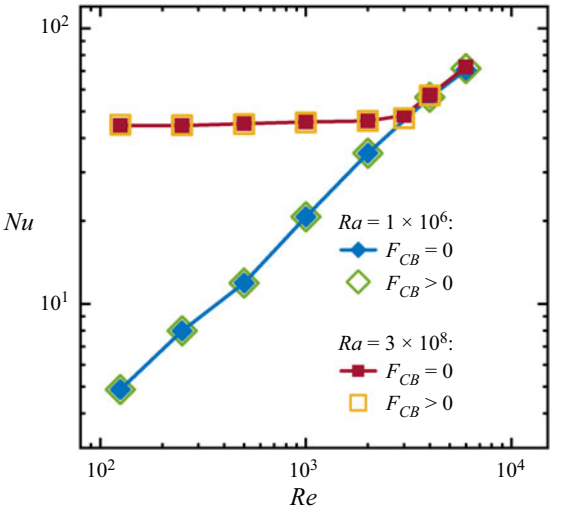


Figure 9. Comparison of heat transfer between the flows without and with the centrifugal buoyancy (F_{CB}) for $Ra = 10^6$ and 3×10^8.

https://doi.org/10.1017/jfm.2021.430 Published online by Cambridge University Press

Ra	Re	R_f	$N_\theta \times N_z \times N_r$	Nu	σ_h	σ_{ϵ_T}	Re_τ	$\frac{L_{max}}{\langle\lambda_k\rangle, \langle\lambda_b\rangle}$	$\Delta r^+_{min}, \Delta r^+_{max}$	t_{u_1}, t_{u_f}
3×10^8	125	0.06	$384 \times 385 \times 97$	3.90	0.99	0.97	13.04	0.29, 0.61	0.12, 0.39	62.15, 257.19
3×10^8	250	0.12	$384 \times 385 \times 97$	7.79	1.00	0.99	19.34	0.42, 0.89	0.18, 0.58	56.58, 117.06
3×10^8	500	0.24	$384 \times 385 \times 97$	11.84	1.00	0.99	30.12	0.63, 1.31	0.28, 0.90	110.86, 114.69
3×10^8	1000	0.48	$384 \times 385 \times 97$	20.68	0.99	1.00	48.27	0.96, 2.01	0.35, 1.59	193.45, 100.06
3×10^8	2000	0.97	$384 \times 385 \times 97$	35.67	0.99	0.97	80.62	1.47, 3.08	0.59, 2.66	325.03, 84.06
3×10^8	3000	1.45	$384 \times 449 \times 113$	46.86	0.98	0.97	110.82	1.72, 3.60	0.69, 3.13	361.91, 62.40
3×10^8	4000	1.93	$512 \times 513 \times 129$	56.11	1.00	0.97	138.76	1.71, 3.59	0.76, 3.43	308.17, 39.85
3×10^8	6000	2.90	$768 \times 721 \times 181$	72.11	0.99	0.97	191.59	1.55, 3.25	0.74, 3.37	60.78, 5.24

Table 7. Summary of results for passive scalar at $Ra = 3 \times 10^8$.

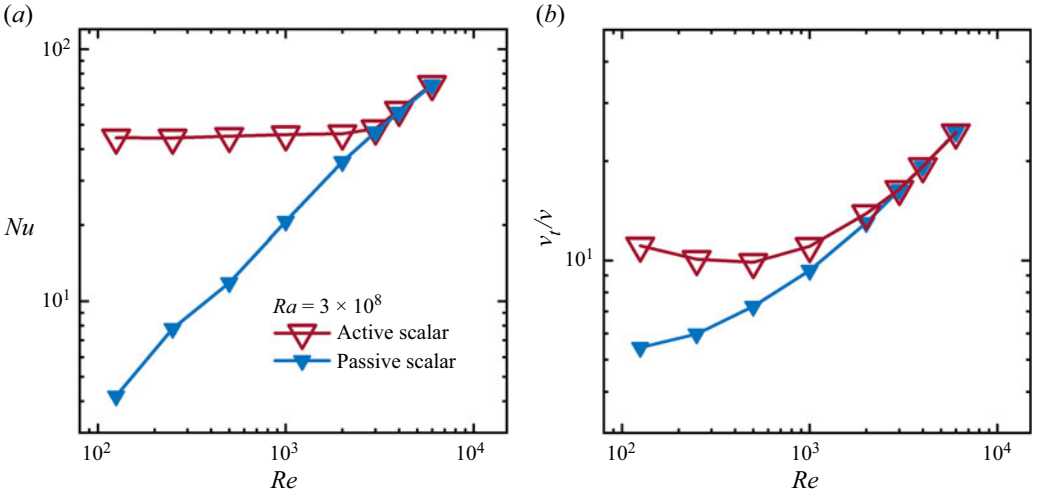


Figure 10. (*a*) Heat transfer Nu and (*b*) dimensionless effective viscosity ν_t/ν of the flows when the temperature fields are treated as active and passive scalars respectively for $Ra = 3 \times 10^8$.

References

Adams, J.C., Swarztrauber, P. & Sweet, R. 1999 Efficient fortran subprograms for the solution of separable elliptic partial differential equations. https://www2.cisl.ucar.edu/resources/legacy/fishpack/.

Ahlers, G., Grossmann, S. & Lohse, D. 2009 Heat transfer and large scale dynamics in turbulent Rayleigh–Bénard convection. *Rev. Mod. Phys.* **81** (2), 503–537.

Akhmedagaev, R., Zikanov, O., Krasnov, D. & Schumacher, J. 2020 Turbulent Rayleigh–Bénard convection in a strong vertical magnetic field. *J. Fluid Mech.* **895**, R4.

Akonur, A. & Lueptow, R.M. 2002 Chaotic mixing and transport in wavy Taylor–Couette flow. *Physica* D **167** (3–4), 183–196.

Akonur, A. & Lueptow, R.M. 2003 Three-dimensional velocity field for wavy Taylor–Couette flow. *Phys. Fluids* **15** (4), 947–960.

Andereck, C.D., Liu, S.S. & Swinney, H.L. 1986 Flow regimes in a circular Couette system with independently rotating cylinders. *J. Fluid Mech.* **164**, 155–183.

Batchelor, G.K. 1959 Small-scale variation of convected quantities like temperature in turbulent fluid. Part 1. General discussion and the case of small conductivity. *J. Fluid Mech.* **5** (1), 113–133.

Bergman, T.L., Incropera, F.P., DeWitt, D.P. & Lavine, A.S. 2011 *Fundamentals of Heat and Mass Transfer*. John Wiley & Sons.

Bilson, M. & Bremhorst, K. 2007 Direct numerical simulation of turbulent Taylor–Couette flow. *J. Fluid Mech.* **579**, 227–270.

https://doi.org/10.1017/jfm.2021.430 Published online by Cambridge University Press

BLASS, A., ZHU, X.J., VERZICCO, R., LOHSE, D. & STEVENS, R.J.A.M. 2020 Flow organization and heat transfer in turbulent wall sheared thermal convection. *J. Fluid Mech.* **897**, A22.

BRADSHAW, P. 1969 The analogy between streamline curvature and buoyancy in turbulent shear flow. *J. Fluid Mech.* **36** (1), 177–191.

BUSSE, F.H. 2012 The twins of turbulence research. *Physics* **5**, 4.

CHANDRASEKHAR, S. 1981 *Hydrodynamic and Hydromagnetic Stability*. Dover Publications.

CHILLÀ, F. & SCHUMACHER, J. 2012 New perspectives in turbulent Rayleigh–Bénard convection. *Eur. Phys. J.* E **35** (7), 1–25.

CHONG, K.L., YANG, Y.T., HUANG, S.D., ZHONG, J.Q., STEVENS, R.J.A.M., VERZICCO, R., LOHSE, D. & XIA, K.Q. 2017 Confined Rayleigh–Bénard, rotating Rayleigh–Bénard, and double diffusive convection: a unifying view on turbulent transport enhancement through coherent structure manipulation. *Phys. Rev. Lett.* **119** (6), 064501.

DONG, S. 2007 Direct numerical simulation of turbulent Taylor–Couette flow. *J. Fluid Mech.* **587**, 373–393.

DUBRULLE, B. & HERSANT, F. 2002 Momentum transport and torque scaling in Taylor–Couette flow from an analogy with turbulent convection. *Eur. Phys. J.* B **26** (3), 379–386.

ECKHARDT, B., GROSSMANN, S. & LOHSE, D. 2007 Torque scaling in turbulent Taylor–Couette flow between independently rotating cylinders. *J. Fluid Mech.* **581**, 221–250.

EMRAN, M.S. & SCHUMACHER, J. 2008 Fine-scale statistics of temperature and its derivatives in convective turbulence. *J. Fluid Mech.* **611**, 13–34.

FARDIN, M.A., PERGE, C. & TABERLET, N. 2014 "The hydrogen atom of fluid dynamics" – introduction to the Taylor–Couette flow for soft matter scientists. *Soft Matt.* **10** (20), 3523–3535.

FROITZHEIM, A., MERBOLD, S., OSTILLA-MÓNICO, R. & EGBERS, C. 2019 Angular momentum transport and flow organization in Taylor–Couette flow at radius ratio of $\eta = 0.357$. *Phys. Rev. Fluids* **4**, 084605.

GROSSMANN, S. & LOHSE, D. 2000 Scaling in thermal convection: a unifying theory. *J. Fluid Mech.* **407**, 27–56.

GROSSMANN, S., LOHSE, D. & SUN, C. 2016 High-Reynolds number Taylor–Couette turbulence. *Annu. Rev. Fluid Mech.* **48** (1), 53–80.

GRÖTZBACH, G. 1983 Spatial resolution requirements for direct numerical simulation of the Rayleigh–Bénard convection. *J. Comput. Phys.* **49** (2), 241–264.

GUILLERM, R., KANG, C., SAVARO, C., LEPILLER, V., PRIGENT, A., YANG, K.-S. & MUTABAZI, I. 2015 Flow regimes in a vertical Taylor–Couette system with a radial thermal gradient. *Phys. Fluids* **27** (9), 094101.

JI, H.T., BURIN, M., SCHARTMAN, E. & GOODMAN, J. 2006 Hydrodynamic turbulence cannot transport angular momentum effectively in astrophysical disks. *Nature* **444** (7117), 343–346.

KANG, C., MEYER, A., MUTABAZI, I. & YOSHIKAWA, H.N. 2017 Radial buoyancy effects on momentum and heat transfer in a circular Couette flow. *Phys. Rev. Fluids* **2**, 053901.

KANG, C., YANG, K.-S & MUTABAZI, I. 2015 Thermal effect on large-aspect-ratio Couette–Taylor system: numerical simulations. *J. Fluid Mech.* **771**, 57–78.

KATAOKA, K. & TAKIGAWA, T. 1981 Intermixing over cell boundary between Taylor vortices. *AIChE J.* **27** (3), 504–508.

KAYS, W.M. & CRAWFORD, M.S. 1980 *Convective heat and mass transfer*. McGraw-Hill.

KING, E.M. & AURNOU, J.M. 2015 Magnetostrophic balance as the optimal state for turbulent magnetoconvection. *Proc. Natl Acad. Sci.* **112** (4), 990–994.

KIRILLOV, O.N. & MUTABAZI, I. 2017 Short-wavelength local instabilities of a circular Couette flow with radial temperature gradient. *J. Fluid Mech.* **818**, 319–343.

KOSCHMIEDER, E.L. 1993 *Bénard cells and Taylor vortices*. Cambridge University Press.

KRASNOV, D., THESS, A., BOECK, T., ZHAO, Y. & ZIKANOV, O. 2013 Patterned turbulence in liquid metal flow: computational reconstruction of the hartmann experiment. *Phys. Rev. Lett.* **110**, 084501.

KRASNOV, D., ZIKANOV, O. & BOECK, T. 2011 Comparative study of finite difference approaches in simulation of magnetohydrodynamic turbulence at low magnetic Reynolds number. *Comput. Fluids* **50** (1), 46–59.

LATHROP, D.P., FINEBERG, J. & SWINNEY, H.L. 1992*a* Transition to shear-driven turbulence in Couette–Taylor flow. *Phys. Rev.* A **46** (10), 6390.

LATHROP, D.P., FINEBERG, J. & SWINNEY, H.L. 1992*b* Turbulent flow between concentric rotating cylinders at large Reynolds number. *Phys. Rev. Lett.* **68** (10), 1515.

LENG, X.Y., KOLESNIKOV, Y.B., KRASNOV, D. & LI, B.W. 2018 Numerical simulation of turbulent Taylor–Couette flow between conducting cylinders in an axial magnetic field at low magnetic Reynolds number. *Phys. Fluids* **30** (1), 015107.

https://doi.org/10.1017/jfm.2021.430 Published online by Cambridge University Press

LIM, Z.L., CHONG, K.L., DING, G.Y. & XIA, K.Q. 2019 Quasistatic magnetoconvection: heat transport enhancement and boundary layer crossing. *J. Fluid Mech.* **870**, 519–542.

LOHSE, D. & XIA, K.Q. 2010 Small-scale properties of turbulent Rayleigh–Bénard convection. *Annu. Rev. Fluid Mech.* **42**, 335–364.

MERBOLD, S., BRAUCKMANN, H.J. & EGBERS, C. 2013 Torque measurements and numerical determination in differentially rotating wide gap Taylor–Couette flow. *Phys. Rev.* E **87**, 023014.

OSTILLA-MÓNICO, R., HUISMAN, S.G., JANNINK, T.J.G., VAN GILS, D.P.M., VERZICCO, R., GROSSMANN, S., SUN, C. & LOHSE, D. 2014 Optimal Taylor–Couette flow: radius ratio dependence. *J. Fluid Mech.* **747**, 1–29.

OSTILLA-MÓNICO, R., VAN DER POEL, E.P, VERZICCO, R., GROSSMANN, S. & LOHSE, D. 2014 Exploring the phase diagram of fully turbulent Taylor–Couette flow. *J. Fluid Mech.* **761**, 1–26.

POPE, S.B. 2000 *Turbulent Flows*. Cambridge University Press.

SCAGLIARINI, A., GYLFASON, Á. & TOSCHI, F. 2014 Heat-flux scaling in turbulent Rayleigh–Bénard convection with an imposed longitudinal wind. *Phys. Rev.* E **89** (4), 043012.

SCHEEL, J.D., EMRAN, M.S. & SCHUMACHER, J. 2013 Resolving the fine-scale structure in turbulent Rayleigh–Bénard convection. *New J. Phys.* **15** (11), 113063.

SHISHKINA, O., STEVENS, R.J.A.M., GROSSMANN, S. & LOHSE, D. 2010 Boundary layer structure in turbulent thermal convection and its consequences for the required numerical resolution. *New J. Phys.* **12** (7), 075022.

SHRAIMAN, B.I. & SIGGIA, E.D 1990 Heat transport in high-Rayleigh-number convection. *Phys. Rev.* A **42** (6), 3650.

SINGH, H., BONNESOEUR, A., BESNARD, H., HOUSSIN, C., PRIGENT, A., CRUMEYROLLE, O. & MUTABAZI, I. 2019 A large thermal turbulent Taylor–Couette (THETACO) facility for investigation of turbulence induced by simultaneous action of rotation and radial temperature gradient. *Rev. Sci. Instrum.* **90** (11), 115112.

STEVENS, R.J.A.M., VAN DER POEL, E.P., GROSSMANN, S. & LOHSE, D. 2013 The unifying theory of scaling in thermal convection: the updated prefactors. *J. Fluid Mech.* **730** (5), 295–308.

STEVENS, R.J.A.M., VERZICCO, R. & LOHSE, D. 2010 Radial boundary layer structure and Nusselt number in Rayleigh–Bénard convection. *J. Fluid Mech.* **643**, 495–507.

TAYLOR, G.I. 1923 Stability of viscous liquid contained between two rotating cylinders. *Phil. Trans. R. Soc. Lond.* **223**, 289–343.

VAN DER VEEN, R.C.A., HUISMAN, S.G., MERBOLD, S., HARLANDER, U., EGBERS, C., LOHSE, D. & SUN, C. 2016 Taylor–Couette turbulence at radius ratio $\eta = 0.5$: scaling, flow structures and plumes. *J. Fluid Mech.* **799**, 334–351.

WEN, J., ZHANG, W.-Y., REN, L.-Z., BAO, L.-Y., DINI, D., XI, H.D. & HU, H.-B. 2020 Controlling the number of vortices and torque in Taylor–Couette flow. *J. Fluid Mech.* **901**, A30.

YOSHIKAWA, H.N., NAGATA, M. & MUTABAZI, I. 2013 Instability of the vertical annular flow with a radial heating and rotating inner cylinder. *Phys. Fluids* **25** (11), 114104.

ZHONG, J.Q., STEVENS, R.J.A.M., CLERCX, H.J.H., VERZICCO, R., LOHSE, D. & AHLERS, G. 2009 Prandtl-, Rayleigh-, and Rossby-number dependence of heat transport in turbulent rotating Rayleigh–Bénard convection. *Phys. Rev. Lett.* **102** (4), 044502.

ZHU, X., JIANG, L.F., ZHOU, Q. & SUN, C. 2019 Turbulent Rayleigh–Bénard convection in an annular cell. *J. Fluid Mech.* **869**, R5.

https://doi.org/10.1017/jfm.2021.430 Published online by Cambridge University Press